



**HAL**  
open science

# Cross-hatched groove influence on the load carrying capacity of parallel surfaces with random roughness

W. Ma, N. Biboulet, A.A. Lubrecht

► **To cite this version:**

W. Ma, N. Biboulet, A.A. Lubrecht. Cross-hatched groove influence on the load carrying capacity of parallel surfaces with random roughness. *Tribology International*, 2021, 153, pp.106610 -. 10.1016/j.triboint.2020.106610 . hal-03491208

**HAL Id: hal-03491208**

**<https://hal.science/hal-03491208>**

Submitted on 8 Sep 2022

**HAL** is a multi-disciplinary open access archive for the deposit and dissemination of scientific research documents, whether they are published or not. The documents may come from teaching and research institutions in France or abroad, or from public or private research centers.

L'archive ouverte pluridisciplinaire **HAL**, est destinée au dépôt et à la diffusion de documents scientifiques de niveau recherche, publiés ou non, émanant des établissements d'enseignement et de recherche français ou étrangers, des laboratoires publics ou privés.



Distributed under a Creative Commons Attribution - NonCommercial 4.0 International License

**s46<sup>th</sup> Leeds-Lyon Symposium on Tribology - September 2-4, 2019, Lyon, France**

**CROSS-HATCHED GROOVE INFLUENCE ON THE LOAD CARRYING CAPACITY OF PARALLEL SURFACES WITH RANDOM ROUGHNESS**

**W. Ma<sup>a</sup>, N. Biboulet<sup>b</sup>, A.A. Lubrecht<sup>b\*</sup>**

<sup>a</sup> Jiangsu Normal University, School of Mechatronic Engineering, Xuzhou, 221116, PRC

<sup>b</sup> Université de Lyon, INSA-Lyon, LaMCoS, CNRS UMR 5259, Villeurbanne F69621, France

**ABSTRACT**

For parallel surfaces, i.e. the oil control ring, the micro-geometry completely determines the hydrodynamic lubrication (HL).

The cross-hatched grooves provide a certain load carrying capacity (LCC) and the surface (plateau) roughness can be an additional source. This paper extends earlier work to numerically solve the hydrodynamic pressure and LCC of parallel surfaces with random roughness and/or grooves. The influence of the groove spacing, width and depth on the LCC is studied.

Results show that the larger the groove spacing, the higher the LCC. Grooves generate a large part of the LCC when the plateau roughness is small. However, for rough surfaces, grooves decrease the LCC and the wider or the deeper the grooves, the larger the decrease of the LCC.

**KEYWORDS**

**Cross-hatched grooves; parallel surfaces; oil control ring; load carrying capacity; hydrodynamic lubrication**

---

\* Corresponding author.  
Email address: [ton.lubrecht@insa-lyon.fr](mailto:ton.lubrecht@insa-lyon.fr)

## Notation

$amp$	groove depth
$A$	dimensionless groove depth, $A=amp/L_x$
$cl$	ACL of an isotropic surface
$d$	groove spacing
$D$	dimensionless groove spacing, $D=d / L_x$
$h$	film thickness
$H$	dimensionless film thickness, $H= h / h_0$
$h_0$	nominal film thickness (flying height)
$L_x$	domain length in $x$ direction
$L_y$	domain length in $y$ direction
$N$	dimensionless distance in the direction perpendicular to a groove, $N = d \sin \alpha / r$
$p$	pressure
$P$	dimensionless pressure, $P =p/(12 \eta u_m L_x/h_0^2)$
$p_0$	boundary pressure, the difference between the ambient and cavitation pressure, $p_0=3 \times 10^4$ [Pa]
$r$	groove width
$RMS$	RMS roughness of surface
$u_m$	mean surface velocity, $u_m=0.5$ [m/s]
$x$	coordinate in the direction of sliding
$X$	dimensionless coordinate, $X=x/ L_x$
$y$	coordinate perpendicular to the direction of sliding
$Y$	dimensionless coordinate, $Y=y/ L_x$
$\alpha$	groove angle with respect to the sliding direction $x$
$\eta$	oil viscosity, $\eta=1 \times 10^{-2}$ [Pa · s]
$\theta$	cavitation fraction
$\delta_{p_{max}}$	difference between the maximum pressure and $p_0$
$\Delta P_{MAX}$	dimensionless difference between the maximum pressure and $p_0$
ACL	autocorrelation length
LCC	load carrying capacity, defined as the mean pressure minus $p_a$ .
OCR	oil control ring
RMS	root mean square
'G'	surface with only grooves
'R'	surface with only roughness
'R+G'	surface with roughness and grooves

## 1. Introduction

In internal combustion engines (ICEs), the piston ring-cylinder liner (PRCL) contact is an important source of mechanical friction. Moreover, excessive oil consumption, associated with polluting emissions and early deterioration of particle filters, should be avoided.

The piston ring pack plays a crucial part in both aspects because of its sealing and lubricating functions. An overview can be found in [1-4] where the effects of relative ring location, tension and design, ring conformability, bore distortion, etc. are outlined. Furthermore, the dynamic behavior of

piston and ring is important. Tian [5] studied their effects on friction, wear and oil transport and discussed the influence of bore distortion on oil transport as well. Optimizing the PRCL contact consists of finding a compromise between fuel consumption, lubricant consumption and cylinder liner life (wear or scuffing, see Willn [6]) as a function of the operating conditions (load, speed, viscosity...).

Optimization of the surface topography is one of the main ways to improve the tribological performance of ICEs [7-9] and special attention has been given to the cylinder bore finish [10]. The cylinder-surface micro-geometry is a predominant parameter that influences the film thickness and consequently the tribological performance, i.e. the load carrying capacity. The top ring has a macro-geometry, which determines the hydrodynamic pressure generation and the cylinder-surface micro-geometry (roughness or texturing) alters it somewhat [11]. However, for parallel surfaces, i.e. the OCR, the micro-geometry alone determines the LCC [12,13].

A simple, classical micro-geometry is the cross-hatched pattern obtained by the honing process. Such a surface consists of two principal components: plateaus and valleys (grooves) with depths exceeding the surface roughness [14].

Classical parameters as  $R_a$ ,  $R_q$  or valley/peak statistics may be insufficient to correctly describe complicated micro-geometries. To obtain the hydrodynamic pressure distributions, functional hydrodynamic analysis using statistical methods was proposed, notably the Patir & Cheng method, which lumps the different components of surface microstructures together. This method builds an averaged Reynolds equation with the Patir & Cheng flow factors [15,16]. This method was applied to the hydrodynamic pressure solution for parallel seals with artificially-generated Gaussian random roughness in [17] and for PRCL contacts with laser-textured grooves in [18].

Other methods allow to decouple these components, such as the homogenization method. A mixed lubrication model using homogenization techniques was proposed by Larsson [19] and Sahlin et al. [20]. It uses measured surface topographies by modeling the surface roughness effects at a local scale and then solving the actual lubrication problem at a global level. This model was then used to investigate oil film formation and frictional losses of the PRCL system [21,22].

An alternative method is to numerically solve the Reynolds equation with deterministic surface geometries. Using this method, Tomanik et al. [23] studied the HL pressure and LCC of cylinder bores and piston rings with laser textured surfaces. Chen [24] studied the effect of liner finish on the LCC of a twin-land OCR and found that the plateau roughness is an additional source of the LCC. More recently, the HL pressure and LCC of PRCL contacts has been studied by Tomanik et al. [25] for real surface topographies, by Yin et al. [26] for laser-textured surfaces and by Noutary et al. [27] for artificially textured surfaces.

However, for complex micro-geometries, the deterministic method leads to a long computing times. The use of Multigrid techniques in earlier work by the authors can drastically reduce the calculational costs [11,12,27,28].

For the HL of the OCR, Biboulet et al. [12] theoretically and numerically solved the pressure and analyzed the LCC as a function of the groove geometry (groove density, depth and angle). They found that a moderate depth leads to a higher pressure than deep or shallow grooves and an optimum groove exists for a maximum dimensionless LCC. Noutary et al. [28] studied the influence of the liner groove shape, depth and density on the LCC. Results show that groove depth and density are the important influencing of LCC, whereas the groove shape only has a small influence.

However, these papers do not consider the contribution of the plateau roughness to the LCC, which is also significant [24]. The coupled influence of the groove geometry and the plateau roughness is more complicated. Mezghani et al. [29] investigated the mutual influence of the crosshatch angle and the superficial roughness of honed surfaces on the friction. They found that under mixed lubrication conditions, the friction coefficient decreases with decreasing liner surface roughness for both plateau-honing (PH) (50° honing angle) and helical slide honing (HSH) (130°) honed surfaces and friction is reduced by 36% for PH, compared to HSH. For a larger crosshatch angle, friction is much less sensitive to superficial plateau roughness, the average oil film thickness is more reduced and it is more likely to enter an HL regime.

Similarly, Hu et al. [30] studied the mutual influence of the plateau roughness and the groove texture on the frictional performance of PRCL. The effect of plateau roughness is incorporated at a local scale by the homogenized technique while the valley component is considered at a global scale, see Spencer [31]. They found that for flat rings, wide and sparse grooves improve the tribological performance and there exists an optimum groove depth which minimizes friction.

The current paper studies the hydrodynamic pressure and LCC of a smooth OCR - honed cylinder liner contact, extending the work by Biboulet et al. [13]. The solver originates from [32], using the deterministic method and incorporating a mass-conserving cavitation. As explained by Ausas et al. [33], non mass-conserving models underestimate the cavitation area leading to a poor estimate of the hydrodynamic pressure. Woloszynski et al. [32] developed an efficient algorithm, called Fischer-Burmeister-Newton-Schur (FBNS), for the joint solution of the Reynolds equation with mass-conserving cavitation and the Fischer-Burmeister equation for complementarity. The FBNS code roughly yields a two orders of magnitude reduction in computing time when compared with other mass-conserving cavitation algorithms, such as the augmented iterative Elrod-Adams  $p-\theta$  [34], the exact linear complementarity based on pivoting [35] and the modified switch function  $\phi-g$  [36].

Inspired by the finding of Bouassida et al. [11] that the LCC of the top ring is deteriorated by cross-hatched grooves, this paper aims to quantify the effect of grooves on the LCC, created by the surface roughness for the OCR (flat ring).

However, the plateau roughness varies substantially from one location to another. That is why this paper uses statistical methods to eliminate the random roughness influence.

## 2. Lubrication model

The dimensionless Reynolds equation with cavitation and the Fischer-Burmeister equation are solved simultaneously:

$$\frac{\partial}{\partial X}(H^3 \frac{\partial P}{\partial X}) + \frac{\partial}{\partial Y}(H^3 \frac{\partial P}{\partial Y}) = \frac{\partial((1-\theta)H)}{\partial X} \quad (1)$$

$$P + \theta - \sqrt{P^2 + \theta^2} = 0 \quad (2)$$

where  $H$  is the gap;  $P$  is the pressure;  $\theta$  is the cavitation fraction;  $X$  is the sliding direction;  $Y$  is perpendicular to  $X$ . Eq. (2) indicates the complementarity condition:  $\theta = 0$  and  $P > 0$ ;  $0 < \theta < 1$  and  $P = 0$ .

In this paper the dimensionless parameters are denoted by capital letters. The dimensional ones are represented by the corresponding lowercase letters.

A Dirichlet condition:  $p=p_a$  is imposed on the boundaries.  $p_a$  is the difference between the ambient

pressure and the cavitation pressure. The specific LCC is defined as (equivalent to) the mean pressure minus  $p_a$ .

Using finite difference techniques, the equations above are discretized and a local linearisation (using Jacobian matrix) is implemented. A grid refinement strategy is used to quickly converge the cavitation boundaries. The implementation and the validation of the numerical solver are detailed in [13].

### 3. Results

#### 3.1. Pressure distribution

Two types of artificially generated surfaces were studied, illustrated in Fig. 1. ‘R’ refers to a surface with only roughness; ‘R+G’ indicates that the rough surface contains grooves. When the plateau roughness is zero, the surface is called ‘G’.

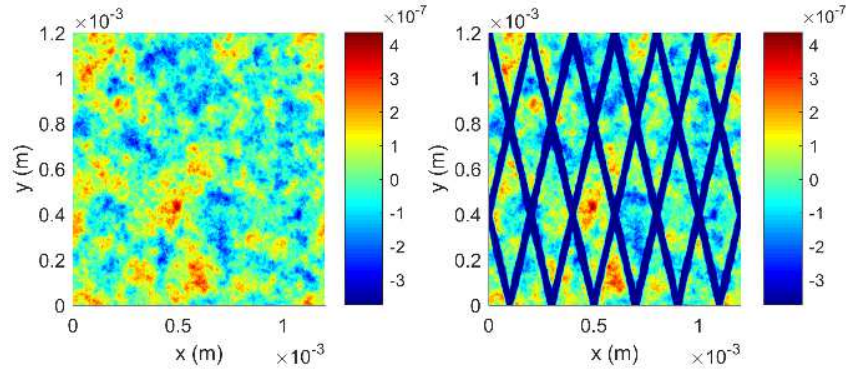


Fig. 1. Generated surfaces: ‘R’ (left) and ‘R+G’ (right),  $d=0.2$ .

The surface roughness is randomly generated, using the algorithm by Patir [37], with a Gaussian height distribution and an exponential autocorrelation function. The groove cross-section has a cosine shape, as used in [11,12] where the groove parameters are detailed. The rough surfaces are considered to be stationary and separated from a smooth sliding surface by a constant distance  $h_0$ , called flying height. Table 1 lists the operating conditions and surface parameters. In this paper, the random roughness has the same autocorrelation length (ACL) in both the  $x$  and  $y$  direction. The ACL is defined as the length at which the integral decays to 10%.

The values in Table 1 are used for the numerical calculations if not stated otherwise.

Table 1. Operating conditions and surface parameters

Operating condition				Surface roughness		Groove			
$h_0$	$p_a$	$\eta$	$u_m$	$L_x(L_y)$	$cl$	$amp$	$r$	$\alpha$	$d$
[ $\mu\text{m}$ ]	[kPa]	[Pa·s]	[m/s]	[mm]	[mm]	[ $\mu\text{m}$ ]	[mm]	[ $^\circ$ ]	[mm]
1	30	0.01	0.5	1.2	0.12	1	0.05	76	0.1, 0.2, 0.3

Fig. 2 shows the groove patterns with the following parameters:  $\alpha=76^\circ$  and  $d=0.1, 0.2, 0.3$  mm, which ensures the intersection at the  $y$ -boundaries. The pressure distributions calculated with the roughness of Fig. 1 ( $d=0.2$  mm for the ‘R+G’) are shown in Fig. 3. One can see that the grooves modify the pressure distribution substantially. Please note that most of the grooves are partially cavitated.

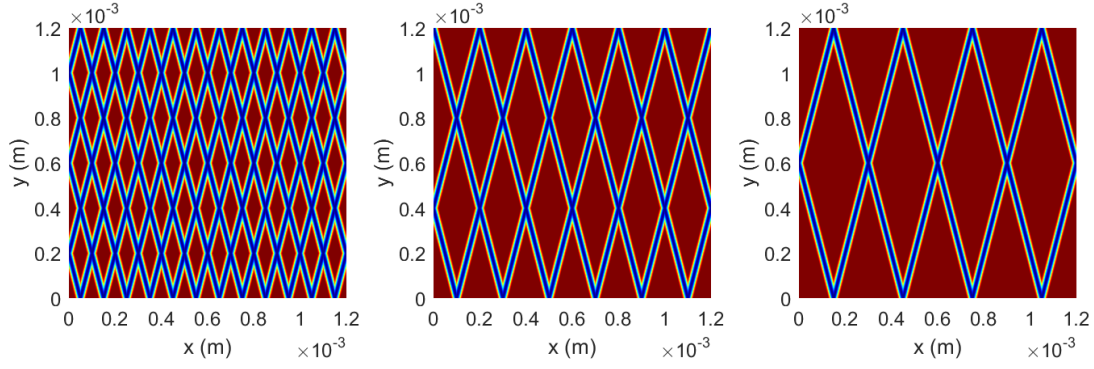


Fig. 2. Groove patterns with a spacing of  $d=0.1$  (left),  $0.2$  (middle),  $0.3$  (right) mm and the inclination angle:  $\alpha=76^\circ$ .

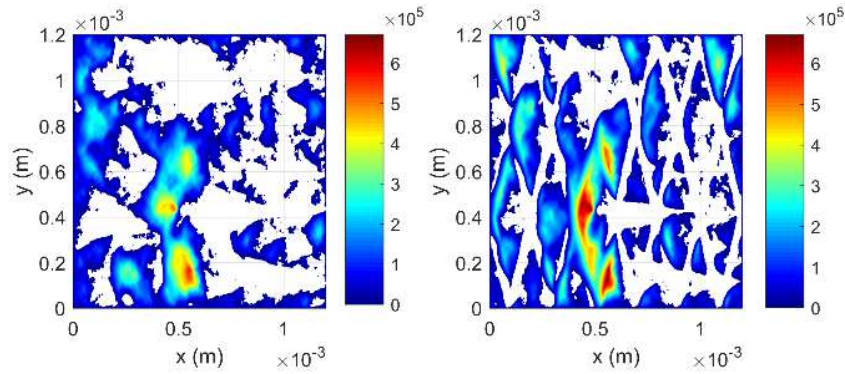


Fig. 3. Pressure distribution for ‘R’ (left) and ‘R+G’ (right),  $d=0.2$ .

### 3.2. Mesh size and accuracy

The accuracy of the numerically calculated LCC (mean pressure) depends on the mesh size. The finer the mesh, the more accurate the solution. Unfortunately, increasing the mesh size increases the computing cost (memory and time). Table 2 compares the LCC results of eight ‘G’ cases on grids with  $2048^2$ ,  $1024^2$  and  $512^2$  points. Some calculations involve very deep ( $amp=3 \mu\text{m}$ ) or very narrow ( $r=0.02 \text{ mm}$ ) grooves.

As expected, the computing time increases with the number of points. The relative difference of grid 512 to grid 1024 is approximately twice that of grid 1024 to grid 2048 except for the first case:  $amp=0.5 \mu\text{m}$  and  $r=0.02 \text{ mm}$ . Based on this observation, one can estimate the numerical error to be first-order. So, the error on a certain grid can be considered to be twice the relative difference with the next finer grid. As the mesh size choice depends on the slope  $amp/r$  [11], Fig. 4 plots the errors as a function of the slope. We consider 10% to be an acceptable error limit. For a depth-width ratio smaller than 0.035, a mesh size of  $512 \times 512$  is appropriate; for a ratio larger than 0.06, one has to use the finest mesh  $2048 \times 2048$ ; for an in-between ratio, one can choose the mesh  $1024 \times 1024$ .

For all the calculations in this paper, we have selected proper grids to obtain an overall error of smaller than 10%.

Table 2. LCC [kPa] for different meshes. Grid (\*): the mesh number of the domain  $(*) \times (*)$ . Rel diff: the LCC difference of the current grid relative to the next finer grid.

$amp$ [ $\mu\text{m}$ ]	0.5	1	1	1.5	2	2.5	2.5	3	Computing
-------------------------	-----	---	---	-----	---	-----	-----	---	-----------

$r$ [mm]	0.02	0.03	0.05	0.05	0.05	0.05	0.04	0.07	time [s]
$amp / r$ [-]	0.025	0.033	0.02	0.03	0.04	0.05	0.063	0.043	
Grid 2048	9.04	23.3	33.6	39.8	40.7	38.9	32.73	42.95	1233
Grid 1024	9.19	23.7	33.8	40.5	41.8	40.3	34.41	44.29	222
Rel diff	1.6%	2.0%	0.7%	1.8%	2.8%	3.8%	5.1%	3.1%	
Grid 512	9.57	24.7	34.2	42.0	44.3	43.5	38.00	47.08	50
Rel diff	4.1%	4.3%	1.4%	3.8%	5.8%	7.8%	10.4%	6.3%	

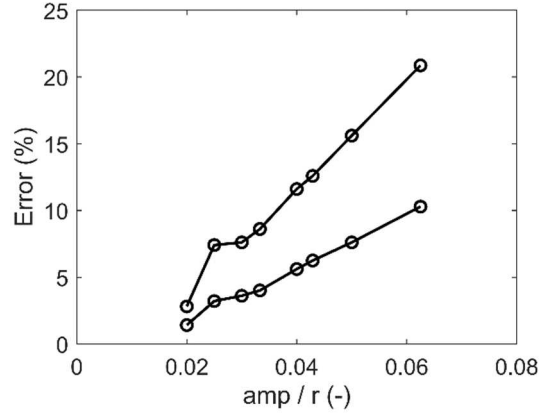


Fig. 4. Accuracy of LCC on grid 512 (top) and 1024 (bottom) as a function of the groove depth-width ratio.

### 3.3. Ensemble study: statistical dispersion

The LCC depends on the random roughness, therefore we study 20 randomly generated rough surfaces and call them an ensemble. Fig. 5 left shows the average LCC of the ensemble as a function of the *RMS* value. The large error bars indicate the standard deviation of the LCC. For an *RMS* larger than  $0.2 \mu\text{m}$  ( $h_0=1 \mu\text{m}$ ), some of the 20 random rough surfaces will show contact spots, which leads to divergence of the solver. The standard deviation for each *RMS* value is large, roughly half the average value. Thus, even though the averaged LCC shows a smooth variation as a function of the *RMS*, it is not possible to conclude on an overall trend.

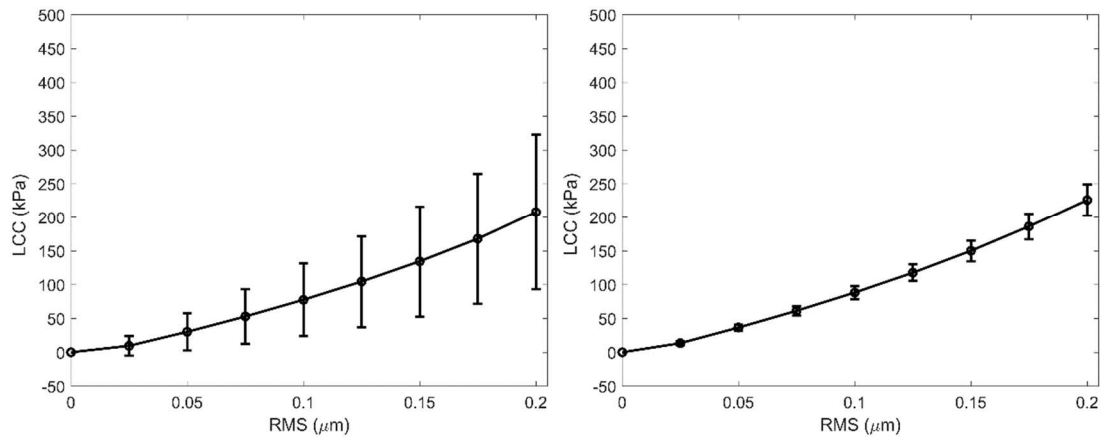


Fig. 5. The average LCC as a function of the *RMS* roughness: one ensemble (left) and averaged over 10 ensembles (right).

Therefore, 10 ensembles are studied statistically. Fig. 5 right shows the average of the 10

ensemble-averaged LCCs as a function of the *RMS* value. The small error bars show that the standard deviation of the 10 ensemble-averaged LCCs is small compared to the average LCC value. Moreover, the trend is very much the same as the one of a single ensemble. This means that 20 surfaces as an ensemble give statistically relevant results. Hence, single-ensemble roughness profiles will be used in the following calculations.

Actually, the LCC as a function of the RMS roughness can be accurately described by the equation:

$$LCC_r = b \cdot RMS^{4/3} \quad (3)$$

One obtains  $b=1723$  with  $R^2=0.998$  for Fig. 5 left and  $b=1800$  with  $R^2=0.999$  for Fig. 5 right, using the LCC in kPa, and *RMS* in  $\mu\text{m}$ .

$b$  depends on the roughness ACF,  $cl$ . Three more cases with  $cl=L_x/40$ ,  $L_x/20$  and  $L_x/5$  are studied. Fig. 6 shows the single ensemble-averaged LCC as a function of the RMS roughness for the four ACFs. The calculations were run on grid 1024 except for  $cl=L_x/40$  on grid 2048, which gives an error of smaller than 5% for all the cases. One can see that the larger the  $cl$  value, the higher the LCC.

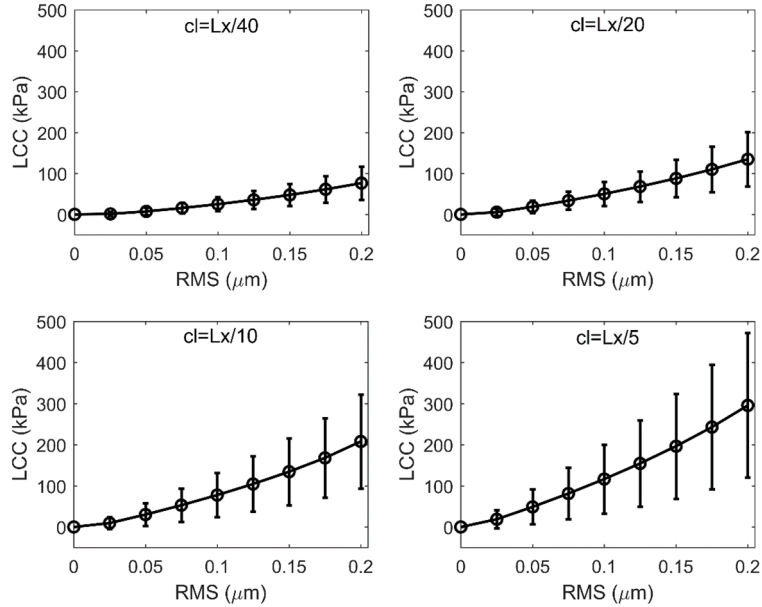


Fig. 6. The average LCC as a function of the RMS roughness for  $cl= L_x/40$ ,  $L_x/20$ ,  $L_x/10$  and  $L_x/5$ .

Table 3 shows the curve-fitting results using Eq. (3). We found that  $b$  is proportional to  $cl^{3/4}$ , with an R-square of 0.997.

Table 3. Curve-fitting results for  $cl= L_x/40$ ,  $L_x/20$ ,  $L_x/10$  and  $L_x/5$  by Eq. (3).

$cl$	$L_x/40$	$L_x/20$	$L_x/10$	$L_x/5$
$b$	614	1122	1720	3000
$R^2$	0.986	0.997	0.997	0.996

Fig. 7 shows the pressure distribution of a single random roughness. The same seed was used to generate the four roughnesses. One can see that the all the pressure distribution patterns are globally the

same. The frequency of the pressure variation depends on the roughness ACF. Of the four cases, the roughness ACF:  $L_x/5$  generates the highest pressure, the biggest pressurized zone (bottom left of the domain) and the largest cavitated area.

The ACF can be seen as the surface wavelength. In earlier work, the authors found that the pressure distribution of a sinusoidal surface is approximately sinusoidal with a phase shift of about  $90^\circ$  and the maximum pressure is proportional to the wavelength. This means that the larger the wavelength, the higher the maximum pressure and the lower the pressure variation frequency.

Any roughness can be decomposed into sinusoidal components. Therefore, a higher-frequency roughness (with a smaller ACF) generates lower pressures, smaller pressurized zones and smaller/more fragmented cavitated zones.

For  $cl = L_x/40, L_x/20, L_x/10$  and  $L_x/5$ , the LCC is 26.8, 45.0, 67.1 and 84.7 kPa and the cavitated area takes up 19%, 28%, 34% and 40% of the total area.

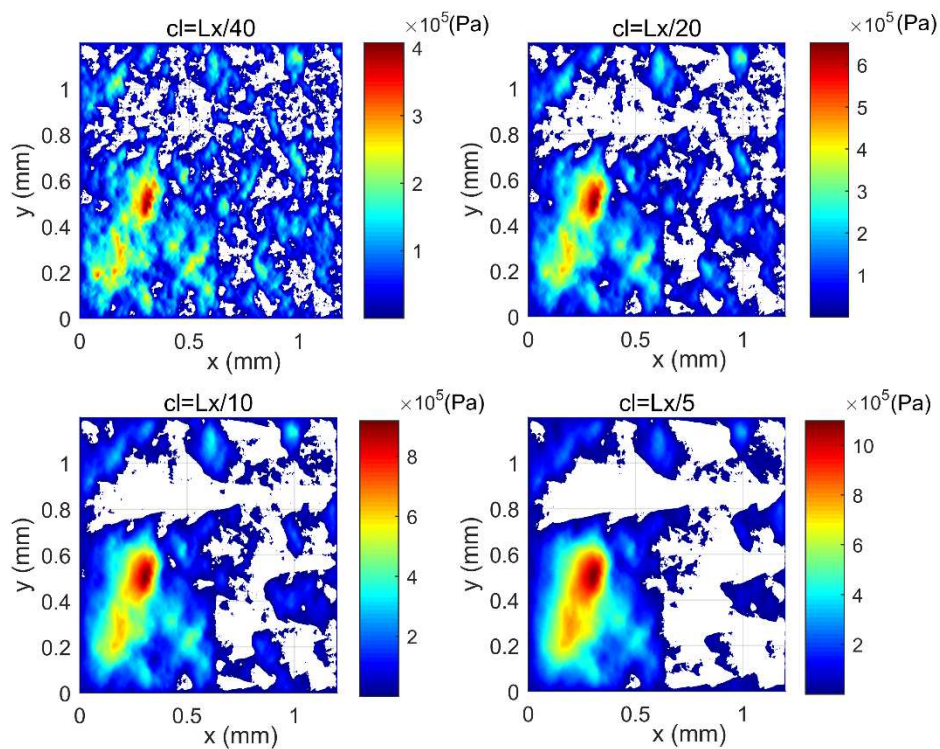


Fig. 7. Pressure distribution with  $RMS=0.1 \mu\text{m}$ ,  $cl = L_x/40, L_x/20, L_x/10$  and  $L_x/5$ . Please note the different color bars.

The following section studies the influence of the groove parameters on the LCC. The LCC for each numerical experiment is averaged over the same ensemble with  $cl=L_x/10$  (as in Fig. 5 left). All R+G cases in the following sections use the same surface roughness with  $RMS=0.15\mu\text{m}$ .

### 3.4. Influence of groove parameters

#### (1) Groove spacing

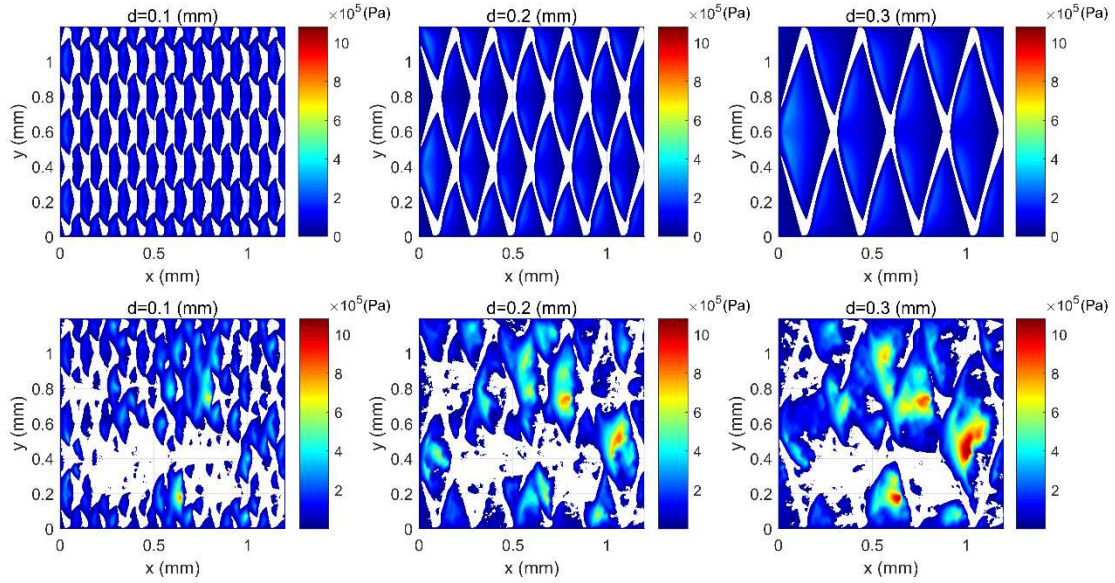


Fig. 8. Pressure distribution with  $r=0.05$  mm (width),  $amp=1$   $\mu\text{m}$  (depth). The first row for groove only surfaces; the second row for 'R+G' surfaces,  $RMS=0.15$   $\mu\text{m}$ . From left to right,  $d=0.1, 0.2, 0.3$  mm.

The first row in Figure 8 is for groove only surfaces. From left to right the LCC is 16.3 kPa, 33.8 kPa, 44.2 kPa and the relative cavitated area is 31.7%, 21.0%, 14.4%. The second row is for the corresponding 'R+G' surfaces. From left to right, the LCC is 29.6 kPa, 64.1 kPa, 99.7 kPa and the relative cavitated area is 41.4%, 35.9%, 29.9%.

Fig. 9 shows the variation of the LCC with the RMS roughness for an 'R' and three 'R+G' surfaces of different groove spacings.

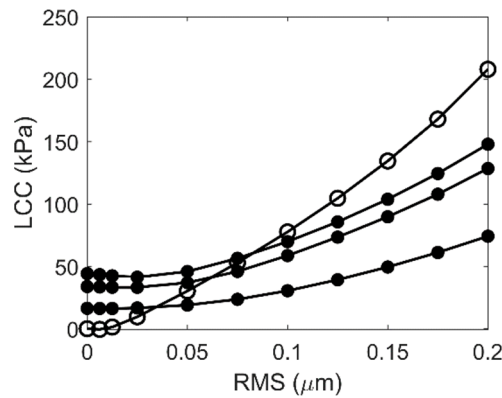


Fig. 9. LCC as a function of the plateau RMS roughness for 'R' (open dots) and for 'R+G' with bottom to top groove spacings  $d=0.1, 0.2, 0.3$  mm (closed dots) and groove depth  $amp=1$   $\mu\text{m}$ .

We observe that for zero roughness, only the grooves generate the LCC and with increasing  $RMS$  (the surface roughness geometry remains the same), the LCC of the 'R+G' remains constant or decreases slightly at low  $RMS$  values and then increases, similar to the LCC of the 'R' surface. The larger the groove spacing (smaller than the domain length), the higher the LCC- $RMS$  curve. The curve for an 'R' surface intersects with those for 'R+G', showing that for small roughness, grooves increase the LCC while for large roughness, grooves decrease the LCC. The grooves serve as channels for oil flowing from high pressure to low pressure zones. This results in a decrease of the LCC, as was

concluded in [11] for contacts with a macroscopic curvature.

(2) Groove width

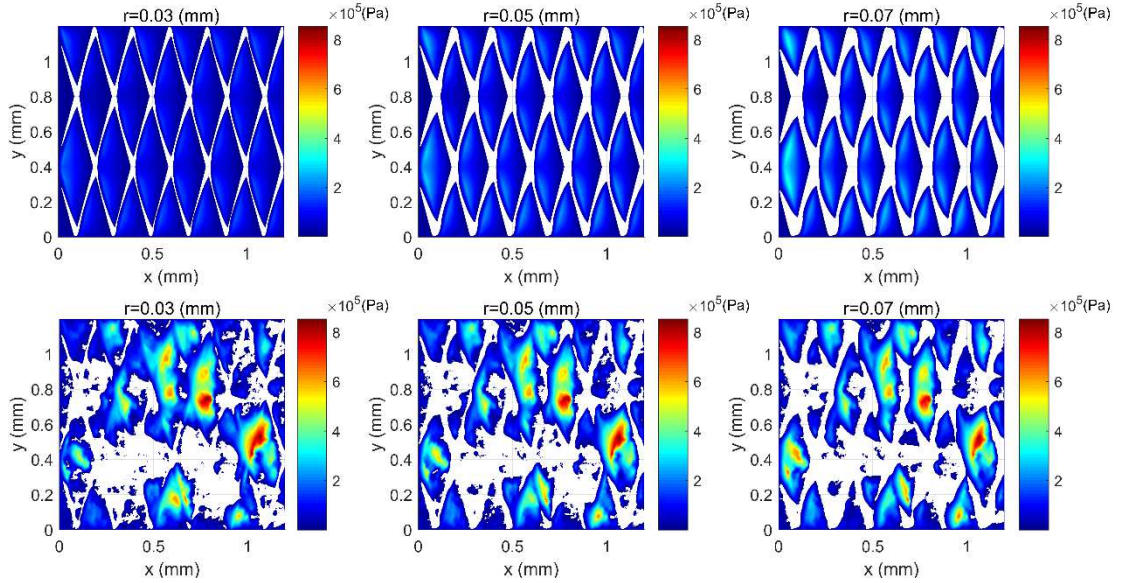


Fig. 10. Pressure distribution with  $d=0.2$  mm (spacing),  $amp=1 \mu m$  (depth). The first row for groove only surfaces; the second row for 'R+G' surfaces,  $RMS=0.15 \mu m$ . From left to right,  $r=0.03, 0.05, 0.07$ mm (width) .

The first row in Figure 10 is for groove only surfaces. From left to right, the LCC is 23.7 kPa, 33.8 kPa, 38.7 kPa and the relative cavitated area is 11.6%, 21.0%, 29.2%. The second row is for the corresponding 'R+G' surfaces. From left to right, the LCC is 69.2 kPa, 64.1 kPa, 61.1 kPa and the relative cavitated area 32.9%, 35.9%, 39.3%.

Fig. 11 shows the variation of the LCC with the RMS roughness for an 'R' and three 'R+G' surfaces with different groove widths. Similarly, one finds that the grooves generate most of the LCC for low-RMS cases and that for a large RMS the LCC increases with the RMS roughness. Furthermore, one can see that for a smaller width, the LCC-RMS curve rises more rapidly. Roughly for each distance  $d$ , beyond the intersection of the LCC-RMS curves of the 'R' and 'R+G', the wider the grooves the lower the LCC, that is, the grooves deteriorate the LCC of the rough surfaces more and more. The reason is the same as explained above: the grooves serve as channels that reduce the pressure generated by the large roughness.

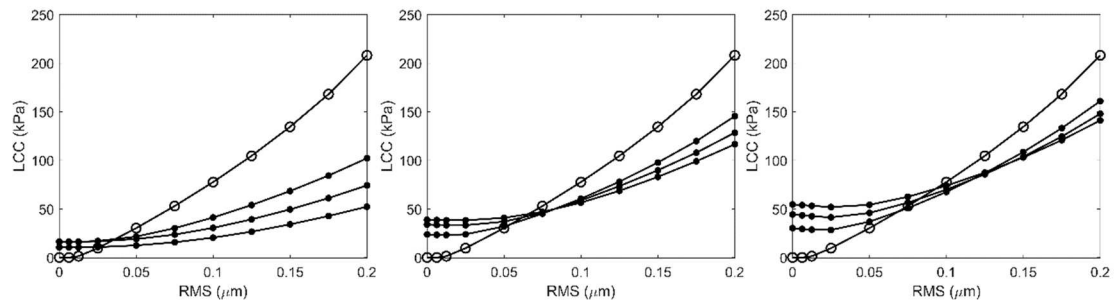


Fig. 11. LCC as a function of the plateau RMS roughness for ‘R+G’ (closed dots) with groove spacing:  $d=0.1$  (left),  $0.2$  (middle),  $0.3$  (right) mm. In each graph, from top to bottom (on the right side) groove width:  $r=0.03, 0.05, 0.07$  mm, with the curve for ‘R’ (open dots) as a reference.

Fig. 12 left (right) shows the variation of the LCC (the maximum pressure  $\delta p_{max}$ ) at  $RMS=0$  with the groove width. One finds that with increasing width, the LCC increases and then decreases. The maximum occurs when the width-spacing ratio is about 0.4, shown in Fig. 12 left. For the same groove width, the larger the spacing, the higher the maximum pressure and the LCC. This is because a large plateau creates a high pressure over a large zone and consequently a large LCC [27].

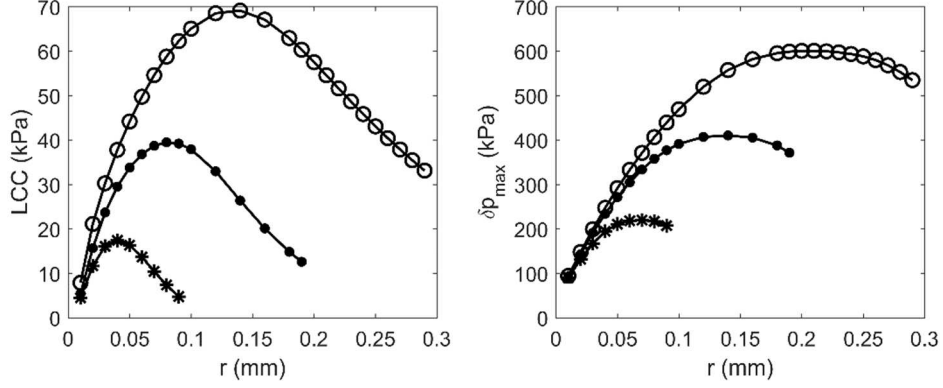


Fig. 12. LCC (left) and maximum pressure (right) of ‘G’ as a function of the groove width.  $amp=1 \mu m$  and  $d=0.1$  (\*),  $0.2$  (.),  $0.3$  (o) mm.

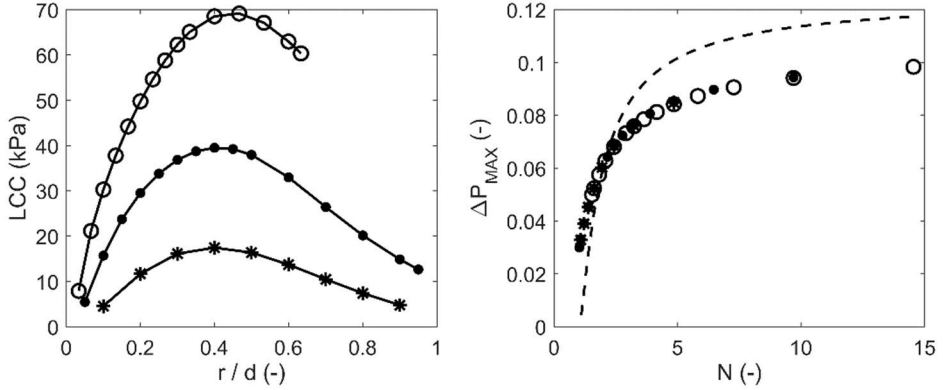


Fig. 13. LCC (left) as a function of the groove width-spacing ratio; dimensionless maximum pressure  $\Delta P_{MAX}$  (right) as a function of  $N$ , compared with the theoretical trend (dashed line) from Eq. (3).  $amp=1 \mu m$  and  $d=0.1$  (\*),  $0.2$  (.),  $0.3$  (o) mm.

Biboulet et al. [12] derived a 1D simplified model for the maximum pressure as a function of the groove depth and the spacing in dimensionless form, described by:

$$\Delta P_{MAX} = \frac{A(A(N-1) + N - \frac{1}{2})^2}{(1+A)((1+A)(N-1)+1)(2(N-1)(1+A)^2 + A+2)} \quad (3)$$

where  $A$  is the dimensionless depth,  $A = amp/h_0$ ;  $N$  is the dimensionless distance in the direction

perpendicular to a groove,  $N = d \sin \alpha / r$ .

Fig. 13 right shows the theoretical variation of  $\Delta P_{MAX}$  with  $N$ , compared with the numerical results. These results have been adjusted by a pre-factor of  $L_x/r$  because of the different dimensionless parameters. One can see that all the data from the numerical experiments of Fig. 12 right fall onto a single curve. The 1D theoretical model cannot approximate the cross-hatched groove structure and it uses triangular grooves, periodical boundary conditions and a non-cavitation hypothesis. This possibly explains the difference with the numerical results. However, the 1D theoretical results show the same trend as our 2D numerical results.

### (3) Groove depth

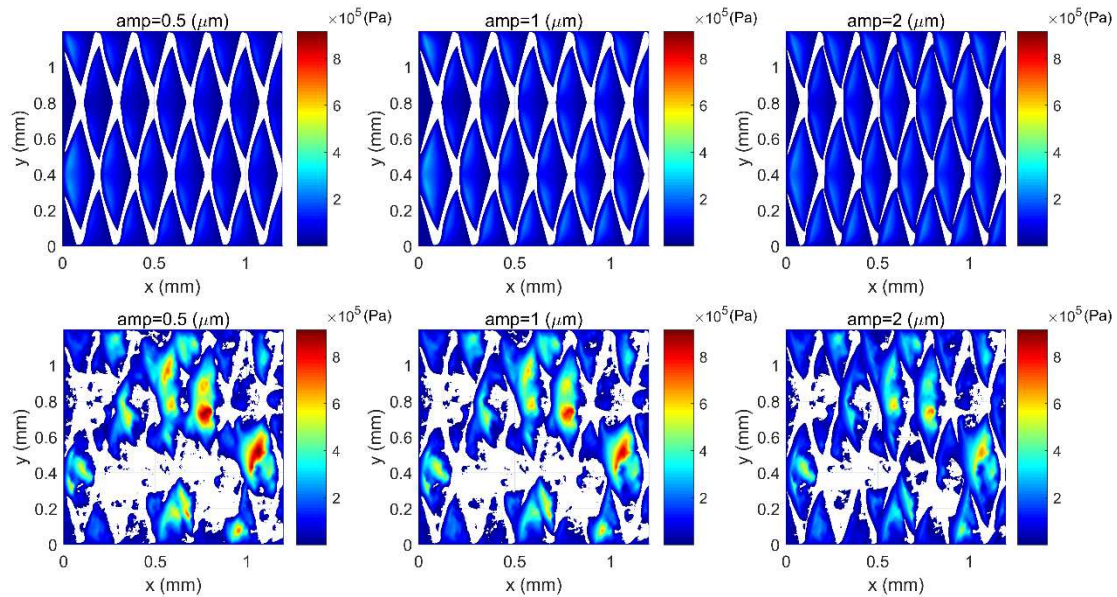


Fig. 14. Pressure distribution with  $d=0.2$  mm (spacing),  $r=0.05$  mm (width). The first row for groove only surfaces; the second row for 'R+G' surfaces,  $RMS=0.15$  μm. From left to right,  $amp=0.5, 1, 2$  μm.

The first row is for groove only surfaces. From left to right, the LCC is 21.3kPa, 33.8 kPa, 41.8kPa and the relative cavitated area is 22.5%, 21.0%, 15.7%.The second row is for the corresponding 'R+G' surfaces. From left to right, the LCC is 73.1 kPa, 64.1 kPa, 53.6 kPa and the relative cavitated area is 36.3%, 35.9%, 30.4%.

We observe a similar LCC versus *RMS* behavior as in Figs. 6 and 7 for four more groove depths ( $amp=0.5, 1.5, 2, 2.5$  μm), shown in Fig. 16. One can see that with increasing groove depth, the curves tend to flatten. This is due to the deeper grooves dominating the plateau roughness influence.

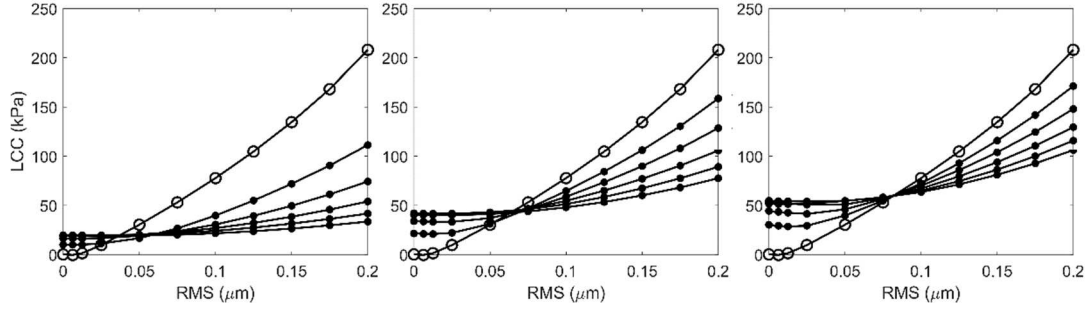


Fig. 15. LCC as a function of the plateau RMS roughness for ‘R+G’ (open dots) with  $d=0.1$  (left),  $0.2$  (middle),  $0.3$  (right) mm. In each graph, from top to bottom (on the right side)  $amp = 0.5, 1, 1.5, 2, 2.5 \mu\text{m}$ ; the curve for ‘R’ (open dots) is used as a reference.

We found that the LCC- $RMS$  behavior can be accurately described by:

$$LCC_{R+G} = \sqrt{a^2 + (b * RMS^{4/3})^2} \quad (4)$$

Take the case of  $d=0.2$  mm as an example, the curve fitting results are listed in Table 4. By comparing Eq. (4) to Eq. (2), one finds that  $a$  is the LCC generated only by the grooves and  $RMS^{4/3}$  represents the effect of the roughness.  $b$  depends on both the roughness and groove parameters and decreases with the groove depth.

Table 4. Curve-fitting results for  $d=0.2$  mm by Eq. (4).

$amp$ [ $\mu\text{m}$ ]	$a$ [kPa]	$b$ [kPa $\cdot \mu\text{m}^{-4/3}$ ]	$R^2$
0	0	1723	0.998
0.5	20	1323	0.9995
1	34	1046	0.998
1.5	40	826	0.998
2	42	663	0.998
2.5	40	564	0.9997

The variation of  $a$  (LCC at  $RMS=0$ ) with the groove depth is numerically obtained, shown in Fig. 13 left. It reveals that with increasing groove depth, the LCC increases and decreases when the groove depth exceeds  $2 \mu\text{m}$ . Figure 16 right shows the variation of the dimensionless maximum pressure  $\Delta P_{MAX}$  with the groove depth, compared with the theoretical one. Once again, the two sets do not exactly match. The origin of the difference is the same as mentioned above. However, all the curves have a similar trend. Moreover, they reach their peaks around  $A=1$ , that is,  $amp=1 \mu\text{m}$  ( $h_0=1 \mu\text{m}$ ); the larger the spacing, the higher the maximum pressure and when the spacings are large, the curves are close. Actually, for the theoretical model, with increasing  $N$  (or  $d$ ), all the curves get close to an upper limit. The limit is obtained from Eq. (3) with  $N = +\infty$ , as:  $\Delta P_{MAX} = 0.5A / (1+A)^2$ .

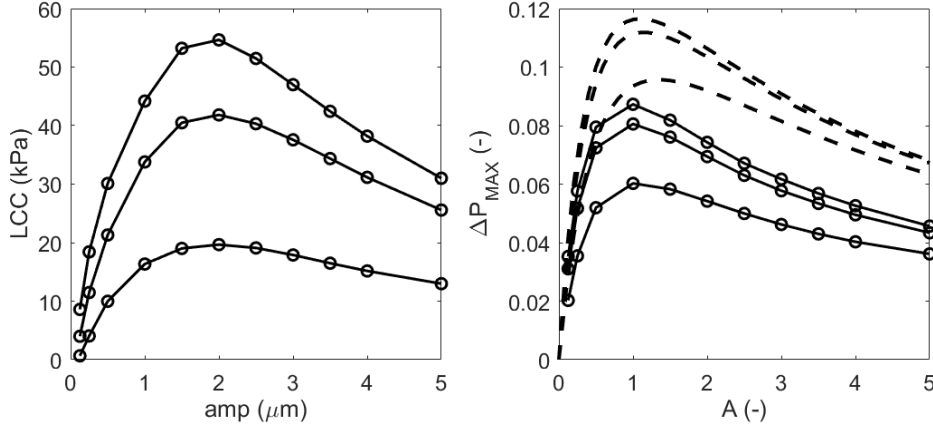


Fig. 16. LCC (left) of the ‘G’ as a function of the groove depth;  $\Delta P_{MAX}$  (right) as a function of the groove depth (open dots) in comparison to the theoretical trends (dashed line) from Eq. (3).  $r=0.05$  mm and bottom to top  $d=0.1, 0.2, 0.3$  mm.

### 3.5. LCC-decreasing behavior with grooves

From the results of the last section, one can see that grooves lead to a decrease of the LCC for a rough surface, which resembles the findings for smooth macroscopically curved surfaces by Bouassida et al. [11].

In accordance with their study, we introduce the same parameters  $f(A)$ ,  $\varepsilon$  and  $\Delta$ :

$$f(A) = \frac{1 + A + 3A^2 / 8}{(1 + A)^{5/2}} \quad (5)$$

$$\varepsilon = \frac{r}{d \sin(\alpha)} \left( 2 - \frac{r}{d \sin(\alpha)} \right) \quad (6)$$

$$\Delta = -\log(\varepsilon) f(A) \quad (7)$$

where  $f(A)$  is the ratio of the flow resistances of a grooved surface and an un-grooved surface;  $\varepsilon$  is called the groove density parameter;  $\Delta$  is a unifying groove parameter. This parameter is composed of the groove depth and groove density (derivations are given in [11]). The lower limit of the relative LCC ( $LCC_{R+G}/LCC_R$ ) is 0 when  $\Delta$  is 0 (the groove depth is infinitely large) and the upper limit is equal to 1 at  $\Delta=+\infty$  (the groove width is infinitely small or the spacing is infinitely large). However, please note that for the finite-size domain used in this work, once the spacing exceeds the domain size, the LCC decreases.

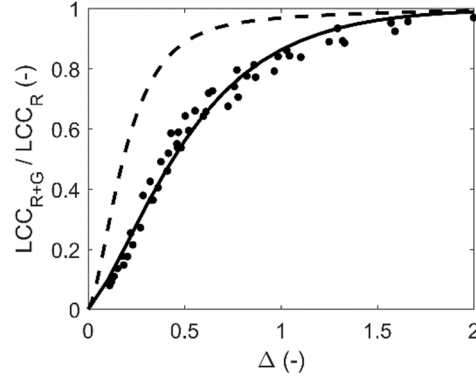


Fig. 17. The relative LCC as a function of  $\Delta$ . Points: Numerical results; solid line: Eq. (8) with  $R^2=0.98$ ; dashed line: Eq. (9) from [11].

We studied the LCC-decreasing behavior at  $RMS=0.175 \mu\text{m}$ . Fig. 14 shows the relative LCC as a function of  $\Delta$ . This plot comprises 50 data points. The groove depth  $amp$  is within  $[0.1, 3.5] \mu\text{m}$ , the groove width  $r$  within  $[0.15, 0.35] \text{mm}$  and the spacing  $d=0.1, 0.2, 0.3 \text{mm}$ .

The best exponential curve fit is obtained by:

$$\frac{LCC_{R+G}}{LCC_R} = 1 - e^{-4.5\Delta} - 2e^{-2.6\Delta} \quad (8)$$

The curve-fitting equation from [11] is

$$\frac{LCC_{R+G}}{LCC_R} = 1 - e^{-9.2\Delta} - e^{-5.4\Delta} - e^{-1.9\Delta} + e^{-13.5\Delta} + e^{-2.1\Delta} \quad (9)$$

Eq. (9) is obtained for macroscopic-curvature cases and based on different boundary conditions. This may explain the difference from Eq. (8).

Another explanation is that we use the ‘R+G’ type for grooved rough surfaces. When  $amp$  is small, the roughness inside the grooves dominates the groove depth. The ideal model should be ‘R/G’, which means the grooves are smooth and the plateau is rough. But the disadvantage of this choice is the possible discontinuity of the surface structure which may lead to other artefacts.

Actually, the unifying parameter is not ideal. For very small groove depths ( $<RMS$ ), the data points will lie far above the curve, Eq. (8). The LCC-decreasing behavior is also influenced by the operating conditions (especially the cavitation pressure) and the roughness parameters (i.e. ACF).

Overall, the current model is a simplified one and its results confirm the earlier findings (for macroscopic-curvature cases).

#### 4. Conclusion

The current paper numerically studies the influence of cross-hatched grooves on the hydrodynamic LCC of a smooth OCR- rough liner surface contact.

For surfaces with random roughness, the LCC increases with the RMS roughness to the power 4/3 and is proportional to the roughness ACF to the power 3/4.

For grooved rough surfaces, the larger the groove spacing, the higher the LCC-RMS curve. Grooves create most of the LCC when the plateau roughness is small. However, for large roughness, grooves decrease the LCC and the wider or the deeper the grooves, the lower the LCC. The grooves serve as channels for oil flowing from high pressure to low pressure zones, resulting in a decrease of the LCC.

The decreasing groove-induced LCC for large surface roughness can be described with a unifying groove parameter  $\Delta$  from Bouassida et al. [11]. When the groove depth is infinitely large,  $\Delta$  is 0 and the relative LCC ( $LCC_{R+G}/LCC_R$ ) reaches 0; when the groove width is infinitely small or the spacing is infinitely large,  $\Delta$  is equal to  $+\infty$  and the relative LCC reaches 1.

## References

- [1] Ma MT, Sherrington I, Smith EH. Analysis of lubrication and friction for a complete piston-ring pack with an improved oil availability model Part 1: circumferentially uniform film. Proc Inst Mech Eng Part J: Eng Tribol 1997; 211: 1–15.
- [2] Ma MT, Sherrington I, Smith EH, Grice N. Development of a detailed model for piston-ring lubrication in IC engines with circular and non-circular cylinder bores. Tribol Int 1997; 30(11): 779–88.
- [3] Mishra PC, Rahnejat H, King PD. Tribology of the ring-bore conjunction subject to a mixed regime of lubrication. Proc Inst Mech Eng Part J: Eng Tribol 2009; 223: 987–98.
- [4] Liu L, Tian T. Modeling piston ring-pack lubrication with consideration of ring structural response. SAE Technical Paper Series 2005, 2005-01-1641: 1-14.
- [5] Tian T. Dynamic behaviors of piston rings and their practical impact. Part 2: oil transport, friction and wear of ring/liner interface and the effects of piston and ring dynamics. Proc Inst Mech Eng Part J: J Eng Tribol 2002; 216: 229–48.
- [6] Willn JE. Characterisation of cylinder bore surface finish—a review of profile analysis. Wear 1972; 19: 143–62.
- [7] Grabon W, Pawlus P, Sep J. Tribological characteristics of one-process and two-process cylinder liner honed surfaces under reciprocating sliding conditions. Tribol Int 2010; 43(10): 1882–92.
- [8] Schommers J, et al. MTZ 07-08/2013. Minimizing friction in combustion engines, vol. 74; 2013.
- [9] Dobrica MB, Fillon M, Pascovici MD, Cicone T. Optimizing surface texture for hydrodynamic lubricated contacts using a mass-conserving numerical approach. Proc Inst Mech Eng Part J: J Eng Tribol 2010; 224: 737–50.
- [10] Tomanik E. Friction and wear bench tests of different engine liner surface finishes. Tribol Int 2008; 41:1032–8.
- [11] Bouassida H, Biboulet N, Sainsot P, Lubrecht AA. Piston ring load carrying capacity: influence of cross-hatching parameters. Proc Inst Mech Eng Part J: J Eng Tribol 2014; 228: 642–8.
- [12] Biboulet N, Bouassida H and Lubrecht AA. Cross hatched texture influence on the load carrying capacity of oil control rings. Tribol Int 2015; 82: 12–19.
- [13] Biboulet N, Lubrecht AA. Efficient solver implementation for Reynolds equation with mass-conserving cavitation. Tribol Int 2018; 118: 295–300.
- [14] Mainsah E, Greenwood JA, Chetwynd DG. Metrology and properties of engineering surfaces. Berlin: Kluwer Academic Publishers 2001; 24: 3–276.
- [15] Patir N, Cheng HS. An average flow model for determining effects of three-dimensional roughness on partial hydrodynamic lubrication. Trans ASME J Tribol 1978; 100: 12–17.
- [16] Patir N, Cheng HS. Application of average flow model to lubrication between rough sliding surfaces. Trans ASME J Tribol 1979; 101: 220–230.
- [17] Harp SR, Salant RF. An average flow model of rough surface lubrication with inter-asperity cavitation. Trans ASME J Tribol 2001; 123: 134–143.

- [18] Profito FJ, Vlădescu S-C, Reddyhoff T, Dini D. Transient experimental and modelling studies of laser-textured. *Tribol Int* 2017; 113: 125–136.
- [19] Larsson R. Modelling the effect of surface roughness on lubrication in all regimes. *Tribol Int* 2009; 42: 512–516.
- [20] Sahlin F, Larsson R, Almqvist A, et al. A mixed lubrication model incorporating measured surface topography. Part 1: Theory of flow factors. *Proc IMechE, Part J: J Eng Tribol* 2010; 224: 335–351.
- [21] Avan EY, Spencer A, Dwyer-Joyce RS, et al. Experimental and numerical investigations of oil film formation and friction in a piston ring–liner contact. *Proc IMechE, Part J: J Eng Tribol* 2013; 227: 126–140.
- [22] Spencer A, Avan EY, Almqvist A, et al. An experimental and numerical investigation of frictional losses and film thickness for four cylinder liner variants for a heavy duty diesel engine. *Proc IMechE, Part J: J Eng Tribol* 2013; 227: 1319–1333.
- [23] Tomanik E, Profito F, Zachariadis D. Modelling the hydrodynamic support of cylinder bore and piston rings with laser textured surfaces. *Tribol Int* 2013; 59: 90–6.
- [24] Chen H. Modeling of liner finish effects on oil control ring lubrication in internal combustion engines based on deterministic method [M.S. thesis]. Massachusetts Institute of Technology; 2008.
- [25] Tomanik E, Mansori ME, Souza R, Profito F. Effect of waviness and roughness on cylinder liner friction. *Tribol Int* 2018; 120: 547–555.
- [26] Yin BF, Xu B, Jia HK, Zhou HQ, Fu YH, Hua XJ. Effects of the array modes of laser-textured micro-dimples on the tribological performance of cylinder liner–piston ring. *Proc IMechE, Part J: J Eng Tribol* 2018; 232(7): 871–881.
- [27] Noutary M–P, Biboulet N, Lubrecht AA. Dimple influence on load carrying capacity of parallel surfaces. *Tribol Int* 2018; Doi: 10.1016/j.triboint.2018.10.033.
- [28] Noutary M–P, Biboulet N, Lubrecht AA. A robust piston ring lubrication solver: Influence of liner groove shape, depth and density. *Tribol Int* 2016; 100: 35–40.
- [29] Mezghani S, Demirci I, Yousfi M, Mansori M. Mutual influence of crosshatch angle and superficial roughness of honed surfaces on friction in ring-pack tribo-system. *Tribol Int* 2013; 66: 54–59.
- [30] Hu Y, Meng X, Xie Y, Fan J, Mutual influence of plateau roughness and groove texture of honed surface on frictional performance of piston ring–liner system, *Proc IMechE, Part J: J Engineering Tribology* 2016, 0(0): 1–22.
- [31] Spencer A, Almqvist A and Larsson R. A semi-deterministic texture-roughness model of the piston ring–cylinder liner contact. *Proc IMechE, Part J: J Eng Tribol* 2011; 225: 325–333.
- [32] Woloszynski T, Podsiadlo P, Stachowiak GW. Efficient solution to the cavitation problem in hydrodynamic lubrication. *Tribol Lett* 2015; 58(1): 18.
- [33] Ausas R, Ragot P, Leiva J, Jai M, Bayada G, Buscaglia G. The impact of the cavitation model in the analysis of microtextured lubricated journal bearings. *Trans ASME J Tribol* 2007; 129: 868–875.
- [34] Ausas RF, Jai M, Buscaglia GC. A mass-conserving algorithm for dynamical lubrication problems with cavitation. *J Tribol* 2009; 131(3): 031702.
- [35] Bertocchi L, Dini D, Giacomini M, Fowell MT, Baldini A. Fluid film lubrication in the presence of cavitation: a mass-conserving two-dimensional formulation for compressible, piezoviscous and non-Newtonian fluids. *Tribol Int* 2013; 67: 61–71.
- [36] Fesanghary M, Khonsari MM. A modification of the switch function in the Elrod cavitation algorithm. *Trans ASME J Tribol* 2011; 133(2): 024501.

[37] Patir N. A numerical procedure for random generation of rough surfaces. *Wear* 1977; 47: 263–277.